YIELDING OF MAGNESIUM: FROM SINGLE CRYSTAL TO POLYCRYSTALLINE AGGREGATES

Stéphane Graff, Wolfgang Brocks, Dirk Steglich

GKSS Research Centre, Institute for Materials Research,

D-21502 Geesthacht, Germany

stephane.graff@gkss.de
wolfgang.brocks@gkss.de
dirk.steglich@gkss.de

ABSTRACT - Hexagonal close-packed (hcp) metals show a deformation behavior, which is quite different from that of materials with cubic crystalline structure. As a consequence, rolled or extruded products of magnesium and its alloys exhibit a strong anisotropy and an unlike yielding in tension and compression. In this work, the microstructural mechanisms of deformation in pure magnesium are modeled by visco-plastic constitutive equations of crystal plasticity. Single crystals and textured polycrystals are analyzed numerically. By means of virtual mechanical tests of representative volume elements mesoscopic yield surfaces are generated. The linking of micro- and mesoscale provides a procedure for the simulation of the yielding and hardening behavior of arbitrarily textured solids with hcp structure such as extruded bars or rolled plates.

Keywords: hcp, magnesium, crystal plasticity, slip systems, twinning, yield surface

INTRODUCTION

Magnesium alloys have attracted attention in recent years as lightweight materials for the transportation industry. Indeed, the low density of magnesium (1.74 g/cm^3) and its relatively high specific strength make it an excellent candidate for applications in transportation industry, where saving of structural weight and reduction of fuel consumption are common challenges, see e.g. Göken et al. (2002), Kainer (2003),

Neelameggham et al. (2005). A broad application of magnesium wrought alloys in modern vehicles and consumer goods requires reliable simulation tools for predicting the forming capabilities, the structural behavior under mechanical loads and the lifetime of the component. The respective constitutive models have to account for several anomalies of the mechanical behavior. Magnesium and its alloys show a pronounced strength differential effect at low homologous temperatures: the tensile strength is much higher than the strength in compression. Furthermore, magnesium exhibits a low ductility as well as strong deformation anisotropy - both demand for non state-of-the-art simulation techniques.

The mentioned mechanical anomalies of magnesium originate from its micromechanical deformation mechanisms, which are determined by its hexagonal close-packed (hcp) crystallographic structure. Metals with hcp crystalline structures hold a reduced number of available slip systems compared to body-centered cubic (bcc) and face-centered cubic (fcc) lattices, making plastic deformation more difficult. With the asymmetric distribution of slip systems over the crystallographic reference sphere, various primary and secondary slip and twinning mechanisms can and have to be be activated at the same time. In contrast, in fcc metals usually only systems of one family become active. Therefore, modelling of the macroscopic deformation of hcp materials requires a careful investigation of the micromechanisms. Understanding the mechanisms of dislocation gliding and deformation twinning for single crystals and polycrystalline aggregates constitutes the fundament for modeling of the macroscopic mechanical behavior. To this end, microstructural experimental observations, mechanical tests and numerical modeling are combined.

Mechanical tests on single crystals of hcp metals for various crystallographic orientations are sophisticated, and the respective literature is scarce. Wonsiewicz and Backofen (1967) as well as Kelley and Hosford (1968a, b) conducted thorough channel-die (plane strain) compression tests on Mg single crystals displaying its complex deformation behavior and revealing the active slip and twinning systems. The data of Kelley and Hosford are used in the present contribution to identify the model parameters of constitutive equations based on crystal plasticity. After a short review of the crystal plasticity model used, the identification of the respective model parameters is

emphasized. In the second part of the contribution, the parameters are applied for predicting the mesoscopic behavior of polycrystalline representative volume elements (RVEs). In this way the microscopic features developing during plastic deformation of Mg are linked to the mesoscale and allow for the prediction of yielding behavior of arbitrarily textured solids, for example extruded bars or rolled plates. RVE calculations can be used to generate macroscopic yield surfaces.

Due to limitations in computational power, simulations of the structural behavior of (macroscopic) polycrystalline structures cannot be performed effectively with models of crystal plasticity. They require phenomenological constitutive equations, e. g. a plastic potential and a flow rule to be used in the framework of rate dependent or rate independent plasticity. The presented method can be used to calibrate parameters of a plastic potential, namely the one recently proposed by Cazacu and Barlat (2004), which accounts for anisotropy and tension/compression asymmetry.

MODELLING OF HCP METALS BY CRYSTAL PLASTICITY

Deformation Mechanisms in Magnesium

Planes and orientations of the hexagonal lattice are described here with the Miller-Bravais indices related to a coordinate system of three basal vectors, $\mathbf{a}_1, \mathbf{a}_2, \mathbf{a}_3$, and the longitudinal axis, $\mathbf{c}$, which is the axis of hexagonal symmetry, see Fig. 1. Within this system, four axes are used rather than three orthogonal ones. Dislocations in a hexagonal lattice may be grouped in three families, $\langle \mathbf{a} \rangle, \langle \mathbf{c} \rangle$ and $\langle \mathbf{a} + \mathbf{c} \rangle$, depending on the orientation of the slip plane and the slip directions, with the respective Burgers vectors of lengths a, c and $\sqrt{a^2 + c^2}$. The basal plane is characterized by its normal vector $\mathbf{n} = \{0001\}$, the prismatic planes by $\mathbf{n} = \{\bar{1}100\}$ and the pyramidal planes by $\mathbf{n} = \{10\bar{1}1\}$ (π1), $\mathbf{n} = \{11\bar{2}2\}$ (π2) and $\mathbf{n} = \{10\bar{1}2\}$ (π3). The corresponding slip directions are equivalent to $\mathbf{m} = \langle 11\bar{2}0 \rangle$ for basal, prismatic and π1 slip. Straining in direction of the c-axis can only be accommodated by $\langle \mathbf{c} + \mathbf{a} \rangle$-systems, with a slip direction of $\langle 11\bar{2}3 \rangle$ for the three pyramidal slip systems, π1, π2 and π3. Beside the deformation caused by slip along crystallographic planes, deformation twinning is an important deformation mechanism for hcp metals. It might be of tensile or compressive

nature, depending whether it results in an elongation or reduction or of the c-axis length. Which of the possible mechanisms will occur depends on the material, the temperature and on the strain rate. In the following, the authors focus on pure magnesium at room temperature. Deformation will be applied in a quasistatic way, such that strain rate effects are negligible.

The knowledge about the relevant deformation mechanism in magnesium has improved over the years. In the first half of the last century the deformation mechanisms at low homologous temperatures were found to be mainly basal slip and pyramidal twinning, see Beck (1939). Later studies, realized in the 50's and 60's by Hauser et al. (1956), Reed-Hill and Robertson (1957) as well as Yoshinaga et al. (1963) revealed prismatic $\langle \mathbf{a} \rangle$ slip systems to be another active slip mode at room temperature. Basal and prismatic slip constitute only four independent shear systems which is not enough for accommodating arbitrary plastic strain. The amount of observed (pyramidal) twinned volume was found not to be sufficient for explaining the ductility of Mg at low temperatures as discussed by Tegart (1964). Slip systems having a deformation component in the $\langle \mathbf{c} \rangle$-direction were considered to play a role in plastic deformation: Stohr and Poirier (1972), Obara et al. (1973) and later Ando and Tonda (2000) have identified pyramidal $\langle \mathbf{a} + \mathbf{c} \rangle$ as an active deformation mechanism at low homologous temperatures.

Modeling activities for better understanding the features of plastic deformation in magnesium alloys started recently and concentrate on the alloy AZ31 and its variation AZ31B as the most common wrought magnesium alloys. Agnew et al. (2001) studied, within others, the relation between mechanical behavior and texture evolution of AZ31B. In order to reproduce similar textures than those observed experimentally, they had to account for $\langle \mathbf{a} + \mathbf{c} \rangle$ slip. Furthermore, the authors concluded that prismatic $\langle \mathbf{a} \rangle$ slip should kept marginal for avoiding undesired effects in the simulated texture. Thus, they have considered only basal, pyramidal $\langle \mathbf{a} + \mathbf{c} \rangle$ and tensile twinning on the $\pi 3$-plane to describe the mechanical behavior simulations of AZ31B. This limitation turned out to be satisfying for simulating uniaxial compression tests of a plate for both, in-plane and through-thickness orientations. In later studies, Agnew et al. (2003) and Agnew and Duygulu (2005) added prismatic $\langle \mathbf{a} \rangle$ slip to the previous set of deformation modes. Non-

basal slip in $\langle \mathbf{a} \rangle$ direction has been shown to be necessary for modeling the in-plane anisotropy of AZ31B rolled plates at low temperatures.

Staroselsky and Anand (2003) described the macroscopic mechanical behavior in tension and compression as well as the respective texture evolution of AZ31B extruded rods and rolled plates without considering any slip system having a deformation component oriented in $\langle \mathbf{c} \rangle$ direction. The considered deformation mechanisms, basal, prismatic, pyramidal $\langle \mathbf{a} \rangle$ and tensile twinning along the $\pi 3$-plane, were enough to get good agreement between experiment and simulation. The systematic texture simulations of AZ31 conducted by Styczynski et al. (2004) showed that the best agreement between simulated and experimental textures is obtained by considering basal, prismatic, pyramidal $\langle \mathbf{a} + \mathbf{c} \rangle$ and tensile twinning, which is the same as in Agnew et al. (2003) and Agnew and Duygulu (2005). Yi et al. (2006) also studied magnesium alloy AZ31 for understanding the relation between texture evolution and flow curves. The authors selected all three $\langle \mathbf{a} \rangle$ slip modes: basal, prismatic, pyramidal, as well as tensile twin and pyramidal $\langle \mathbf{a} + \mathbf{c} \rangle$-slip.

As a resume, the significant deformation mechanisms acting in Mg and its alloys are still subjected to discussion. Generally, the use of any $\langle \mathbf{a} \rangle$ and one $\langle \mathbf{a} + \mathbf{c} \rangle$ slip system family additionally to basal and tensile twinning seems to be necessary. Since pyramidal $\langle \mathbf{a} \rangle$ slip is equivalent to a combination of basal and prismatic $\langle \mathbf{a} \rangle$ cross-slip, this particular system will not be considered in the following calculations. The remaining primary systems, i.e. basal $\langle \mathbf{a} \rangle$, prismatic $\langle \mathbf{a} \rangle$, pyramidal $\langle \mathbf{a} + \mathbf{c} \rangle$ plus tensile twinning on $\{10\bar{1}2\}$ are chosen here to model the mechanical behavior in the framework of crystal plasticity. These families include three basal, three prismatic, six pyramidal and six twinning systems. Table 1 summarizes the deformation modes (families of systems) used in the following.

Table 1: Deformation modes considered in the present work

Name	Number of Slip Systems	Plane	Slip Direction
Basal $\langle \mathbf{a} \rangle$	3	$\{0001\}$	$\langle 11\bar{2}0 \rangle$
Prismatic $\langle \mathbf{a} \rangle$	3	$\{1\bar{1}00\}$	$\langle 11\bar{2}0 \rangle$
Pyramidal $\langle \mathbf{a} + \mathbf{c} \rangle$ (π2)	6	$\{11\bar{2}2\}$	$\langle 11\bar{2}3 \rangle$
Tensile Twin (π3)	6	$\{10\bar{1}2\}$	$\langle 10\bar{1}1 \rangle$

Constitutive Formulations

The kinematical theory for the mechanics of crystals has been established in the pioneering work of Taylor (1938) and the theory by Hill (1966), Rice (1971) , Hill and Rice (1972). The model of crystal plasticity used here employs the framework of Peirce et al. (1982) and Asaro (1983a, b). The implementation in the commercial finite element code ABAQUS is based on the user-material routine of Huang (1991).

The lattice of a crystalline material undergoes elastic stretching, rotation and plastic deformation. The latter is assumed to arise solely from crystalline slip. The total deformation gradient $\mathbf{F}$ is decomposed as

$$\mathbf{F} = \mathbf{F}^* \cdot \mathbf{F}^p , \tag{1}$$

where $\mathbf{F}^p$ denotes plastic shear of the material to an intermediate reference configuration in which lattice orientation and spacing are the same as in the initial configuration, and $\mathbf{F}^* = \mathbf{V}^* \cdot \mathbf{R}^*$ denotes stretching and rotation of the lattice. Superscript * always indicates the lattice part of the kinematic quantities in the following.

The rate of change of $\mathbf{F}^p$ is related to the slip rate $\dot{\gamma}^{(\alpha)}$ of the α slip system by

$$\dot{\mathbf{F}}^p \cdot \mathbf{F}^{p-1} = \sum_\alpha \dot{\gamma}^{(\alpha)} \mathbf{m}^{(\alpha)} \mathbf{n}^{(\alpha)} , \tag{2}$$

where the sum ranges over all activated slips systems, and the unit vectors $\mathbf{m}^{(\alpha)}$, $\mathbf{n}^{(\alpha)}$ are the slip direction and the slip-plane normal, respectively, in both initial and intermediate reference configurations, which transform to

$$\mathbf{m}^{*(\alpha)} = \mathbf{F}^* \cdot \mathbf{m}^{(\alpha)} \quad , \quad \mathbf{n}^{*(\alpha)} = \mathbf{n}^{(\alpha)} \cdot \mathbf{F}^{*-1} \tag{3}$$

in the current deformed configuration, where

$$\mathbf{n}^{*(\alpha)} \cdot \mathbf{m}^{*(\beta)} = \mathbf{n}^{(\alpha)} \cdot \mathbf{F}^{*-1} \cdot \mathbf{F}^* \cdot \mathbf{m}^{(\beta)} = \mathbf{n}^{(\alpha)} \cdot \mathbf{m}^{(\beta)} = \delta_{\alpha\beta}. \tag{4}$$

The velocity gradient in the current configuration is given by

$$\mathbf{L} = \dot{\mathbf{F}} \cdot \mathbf{F}^{-1} = \mathbf{D} + \mathbf{\Omega} . \tag{5}$$

The symmetric stretching rate, $\mathbf{D}$, and the skew vorticity or spin tensor, $\mathbf{\Omega}$, can be decomposed into lattice and plastic parts

$$\mathbf{D} = \mathbf{D}^* + \mathbf{D}^{\mathrm{p}} \quad , \quad \mathbf{\Omega} = \mathbf{\Omega}^* + \mathbf{\Omega}^{\mathrm{p}}, \tag{6}$$

with

$$\mathbf{D}^* + \mathbf{\Omega}^* = \dot{\mathbf{F}}^* \cdot \mathbf{F}^{*-1} \quad , \quad \mathbf{D}^{\mathrm{p}} + \mathbf{\Omega}^{\mathrm{p}} = \sum_\alpha \dot{\gamma}^{(\alpha)} \mathbf{m}^{*(\alpha)} \mathbf{n}^{*(\alpha)} . \tag{7}$$

The elastic properties are assumed to be unaffected by slip, i.e. the stress is determined solely by $\mathbf{F}^*$. Thus, the stretching rate, $\mathbf{D}$, is related to the Jaumann derivative of Cauchy's stress tensor, $\mathbf{T}$, by

$$\overset{\nabla^*}{\mathbf{T}} + \mathbf{T}\left(\mathbf{1} : \mathbf{D}^*\right) = \underline{\underline{\mathbb{C}}} : \mathbf{D}^*, \tag{8}$$

where $\underline{\underline{\mathbb{C}}}$ is the tensor of elastic moduli. The Jaumann rate in eq. (8) is the corotational stress rate on axes that rotate with the crystal lattice, which is related to the corotational stress rate on axes rotating with the material by

$$\overset{\nabla^*}{\mathbf{T}} = \dot{\mathbf{T}} - \mathbf{\Omega}^* \cdot \mathbf{T} + \mathbf{T} \cdot \mathbf{\Omega}^* = \overset{\nabla}{\mathbf{T}} + \left(\mathbf{\Omega} - \mathbf{\Omega}^*\right) \cdot \mathbf{T} - \mathbf{T} \cdot \left(\mathbf{\Omega} - \mathbf{\Omega}^*\right). \tag{9}$$

The crystalline slip is assumed to obey Schmid's law, i.e. the slipping rate $\dot{\gamma}^{(\alpha)}$ depends on $\mathbf{T}$ solely through Schmid's resolved shear stresses,

$$\tau^{(\alpha)} = \mathbf{n}^{*(\alpha)} \cdot \frac{\rho_0}{\rho} \mathbf{T} \cdot \mathbf{m}^{*(\alpha)}, \tag{10}$$

where ρ_0 and ρ are the mass densities in the reference and current states. The rate of

change of the resolved shear stresses is

$$\dot{\tau}^{(\alpha)} = \mathbf{n}^{*(\alpha)} \cdot \left[\overset{\nabla^*}{\mathbf{T}} + \mathbf{T}\left(\mathbf{1}:\mathbf{D}^*\right) - \mathbf{D}^* \cdot \mathbf{T} + \mathbf{T} \cdot \mathbf{D}^* \right] \cdot \mathbf{m}^{*(\alpha)} . \tag{11}$$

According to Peirce et al. (1982), the constitutive equation of slip is assumed as a viscoplastic power law,

$$\frac{\dot{\gamma}^{(\alpha)}}{\dot{\gamma}_0^{(\alpha)}} = \left| \frac{\tau^{(\alpha)}}{\tau_Y^{(\alpha)}} \right|^n \mathrm{sign}\left(\frac{\tau^{(\alpha)}}{\tau_Y^{(\alpha)}} \right), \tag{12}$$

where $\dot{\gamma}_0^{(\alpha)}$ is a reference strain rate. $\tau_Y^{(\alpha)}$ characterizes the current strength of the α slip system, and n is the rate sensitivity exponent. Strain hardening is characterized by the evolution of the strengths

$$\dot{\tau}_Y^{(\alpha)} = \sum_{\beta} h_{\alpha\beta}\left(\overline{\gamma}\right)\dot{\gamma}^{(\alpha)} , \tag{13}$$

with $h_{\alpha\beta}$ being the self ($\alpha = \beta$) and latent ($\alpha \neq \beta$) hardening moduli depending on Taylor's cumulative shear strain on all slip systems,

$$\overline{\gamma} = \sum_{\alpha} \int_0^t \left| \dot{\gamma}^{(\alpha)} \right| d\tau . \tag{14}$$

Slip systems are grouped into four families (Table 1) where twinning is treated like slip, see below. Interactions of the different active systems are handled with respect to the families of systems, not the individual system. It is furthermore assumed that

$$h_{\alpha\alpha} = h(\overline{\gamma}) \text{ and } h_{\alpha\beta} = q_{\alpha\beta} h(\overline{\gamma}), \tag{15}$$

so that the hardening law can be written as

$$\tau_Y^{(\alpha)} = \tau_0 + \int_0^t h(\overline{\gamma})\left(\dot{\gamma}^{(\alpha)} + q_{\alpha\beta} \sum_{\alpha \neq \beta} \dot{\gamma}^{(\beta)} \right) d\tau . \tag{16}$$

with $\tau_0 = \tau_Y^{(\alpha)}(0)$ as integration constant. Hardening parameters as well as the values of the interaction parameters $q_{\alpha\beta}$ have to be calibrated by a fitting procedure considering both, test results of single crystals as well as polycrystals.

Three different hardening laws are applied in the following, namely

- linear hardening,

$$h(\bar{\gamma}) = h_0,$$ (17)

- Voce hardening (Agnew *et al.*, 2001, Yi *et al.*, 2006),

$$h(\bar{\gamma}) = h_0\left(1 - \frac{\tau_0}{\tau_\infty}\right)\exp\left(-\frac{h_0\bar{\gamma}}{\tau_\infty}\right),$$ (18)

with τ_∞ being the saturation stress,

- and particularly for deformation twinning,

$$h(\bar{\gamma}) = \begin{cases} h_0 & for & \gamma \le \gamma_{ref} \\ h_0\left(\dfrac{\bar{\gamma}}{\gamma_{ref}}\right)^{m-1} & for & \gamma > \gamma_{ref} \end{cases}.$$ (19)

The integrated functions of eqns. (17) – (19) presenting the different hardening characteristics are shown in Figure 2. The specific hardening law of eq. (19) was used for the description of deformation twinning in order to model the observed phenomenon of a sudden stress increase due to saturation of twinning after a certain amount of strain has been reached. Twinning is assumed to be geometrical irreversible and the respective systems can be activated by either tension or compression of the **c**-axis, depending on whether the deformation results in an elongation or a shortening of the **c**-orientation. Physically it is connected with a lattice rotation of a finite domain. This effect is difficult to realize within the framework of crystal plasticity. Hence, twinning is handled here as additional slip mechanisms of the type $\{10\bar{1}2\}\langle10\bar{1}1\rangle$ and the reorientation of crystallographic planes due to rotation is not taken into account. This way of representation for twinning assumes that, as twinning has saturated, further plastic deformation issues only in the "untwinned" material. Furthermore, it is assumed that both, slip and twinning, can operate simultaneously at a material point. Deformation twinning modeled as crystallographic slip is supposed to follow Schmid's law, see eqs. (12) - (14). Its hardening law is assumed as in eq. (19), and the polar character of twinning is taken into account with the restriction,

$$\tau_{\mathrm{Y}}^{(\alpha)} \to \infty \quad \text{for} \quad \tau^{(\alpha)} \leq 0 \,, \tag{20}$$

allowing extension of the **c**-orientation (tensile twinning) only.

Test Configurations and FE Models

In order to study the deformation mechanisms other than the easy glide basal slip and tensile twinning, Wonsiewicz and Backofen (1967) as well as Kelley and Hosford (1968a, b) performed plane strain compression tests on pure magnesium single crystals and on textured magnesium samples cut out of a rolled plate. The authors used a channel die experiment (see Figure 2a): small samples (approx. $6 \times 10 \times 13$ mm^3) were compressed in a steel channel in one direction, while the second direction was constrained in displacement (rigid die) and the third one was free in order to realize a plane strain state. By changing the initial orientation of a (textured) sample, different slip and slip/twinning modes can be activated. The experimental results of Kelley and Hosford are used here as a reference.

In the following, the loading direction is denoted as "1" and the constraint direction as "2". Table 2 gives an overview on the respective orientations for the case of the single crystal. The orientations with respect to compression loading and applied constraint for the polycrystalline case are indicated by two of the letters L (longitudinal or rolling), T (transverse) and S (short transverse or thickness), where the first letter denotes the loading direction and the second the constraint direction.

Simulations of single crystal and polycrystalline aggregates presented in the following have been realized in the framework of finite elements using 8-node 3D elements. An equivalent discretisation has been chosen for single crystals and polycrystals: a crystal is described by one single finite element. Consequently, in a polycrystalline specimen the number of modeled grains corresponds with the number of finite elements. A representative volume element (RVE) has to consist of a sufficient large number of grains. However, in order to save computational time, $8 \times 8 \times 8$ grains are considered in the RVE, each represented by an 8-node brick element having its individual material orientation, see Figure 2b. The die and the loading stamp are modeled by rigid surfaces.

Friction between the sample and the rigid surfaces is accounted for, assuming a Coulomb friction coefficient of 0.05 for all tests. In case of the polycrystalline specimen, surfaces in extension direction have not been constrained. All simulations assume isotropic elasticity with Young's modulus E=45000 MPa and Poisson ratio $\nu = 0.3$. Since the experiments have been performed with quasistatic loading, the strain rate sensitivity exponent n in equation (12) is set equal to 50, making the simulation results almost rate independent. The reference strain rate for each slip system, $\dot{\gamma}_0^{(\alpha)}$, is chosen to be compatible with the time scale in the FE simulations, and set to 10^{-3}.

Table 2: Definition of the different orientations used with the plane-strain compression tests on single crystals by Kelley and Hosford (1968a)

test	loading (1)	constraint (2)
A	$\langle 0\,0\,0\,1 \rangle$	$\langle 1\,0\,\bar{1}\,0 \rangle$
B	$\langle 0\,0\,0\,1 \rangle$	$\langle 1\,\bar{2}\,1\,0 \rangle$
C	$\langle 1\,0\,\bar{1}\,0 \rangle$	$\langle 0\,0\,0\,1 \rangle$
D	$\langle 1\,\bar{2}\,1\,0 \rangle$	$\langle 0\,0\,0\,1 \rangle$
E	$\langle 1\,0\,\bar{1}\,0 \rangle$	$\langle 1\,\bar{2}\,1\,0 \rangle$
F	$\langle 1\,\bar{2}\,1\,0 \rangle$	$\langle 1\,0\,\bar{1}\,0 \rangle$
G	$\langle 0\,0\,0\,1 \rangle$ at 45°	$\langle 1\,0\,\bar{1}\,0 \rangle$

In order to evaluate the mechanical response of single and polycrystals the following definitions of true stresses and true (logarithmic) strains are respectively used,

$$\varepsilon_{11} = \left| \ln\left(\frac{l_{11}^0 + \Delta l_{11}}{l_{11}^0} \right) \right| = \left| \ln\left(1 + \frac{\Delta l_{11}}{l_{11}^0} \right) \right|, \tag{21}$$

$$\sigma_{11} = \frac{f}{A_0} F \left(1 + \frac{\Delta l_{11}}{l_{11}^0} \right). \tag{22}$$

Here, l_{11}^0 and A_0 are the RVE's original length in loading direction and original section with respect to loading direction, respectively. F denotes the absolute value of the load

and $f = 0.89$ is the friction correction coefficient introduced by Kelley and Hosford (1968a,b). The above expression for true stresses is obtained in assuming constant volume of the RVE during plastic deformation.

As in the channel die case, the simulations of uniaxial tension and compression tests in L, T and S-direction were performed on polycrystalline aggregates of 8×8×8 solid elements showing the same crystallographic orientations than presented in Fig. 5a. Periodic boundary conditions were applied on the surfaces of the RVE. In order to simulate yield loci and strain hardening in the (L,T)-plane, the plastic deformation of the same polycrystalline aggregate is investigated under plane stress conditions performing radial in-plane loading paths with different ratios of $\sigma_T / \sigma_L = \arctan \rho$, where ρ is the angle to the rolling direction (L) of the plate. For each loading path, several unloading steps have been realized in order to separate elastic and plastic mesoscopic strain.

Deformation of Single Crystals, Textured Polycrystals, and Parameter Identification

Establishing a model is the first significant step, determining its parameters is the second and often more complex one. The more advanced and sophisticated material models are, the more parameters do they include. Their identification requires inverse techniques, in which numerical simulations are calibrated by test data. Various procedures exist for this process, comprising manual fitting, trial and error, numerical optimization and neural networks, see e.g. the review articles of Mahnken (2004), Brocks and Steglich (2006). The determination of numerous parameters raises a lot of fundamental questions, namely on the uniqueness of a parameter set, the sensitivity of the mechanical response to variations of these parameters and the design of adequate tests capable of identifying certain model parameter. Neither of these problems can be elaborated here, as the focus is on the performance of the model and as test data had to be taken from literature. Based on these data, parameter identification has been executed as a systematic trial and error, yielding results that look reasonably but cannot claim to be the best possible fit. Though optimization methods appear as appropriate for obtaining a "best fit", they lack any physical background and evidence. Parameter identification in practice requires insight knowledge of constitutive theories as well as experimental mechanics. Optimization

algorithms and software cannot replace this expertise.

Apart from the material constants for isotropic elasticity, namely Young's modulus and Poisson's ratio, the constitutive model presented above comprises three kinds of parameters per slip system, α,

- two parameters of the viscoplastic law, $\dot{\gamma}_0^{(\alpha)}$ and n, eq. (12),

- between two and four hardening parameters, depending on the respective hardening law, τ_0, τ_∞, h_0, γ_{ref}, m, eqs. (17), (18), (19),

- parameters of latent hardening, describing the interaction between the various slip systems, $q_{\alpha\beta}$, eq. (16).

For simplification, it has been assumed, that direct and latent hardening are identical for all slip systems of each of the four basic mechanisms, namely basal slip, prismatic slip, pyramidal slip and twinning. Linear hardening, eq. (17), with two parameters, τ_0, h_0, is assumed for basal slip, Voce hardening, eq. (18), with three parameters, τ_0, τ_∞, h_0, for prismatic and pyramidal slip, and the combination of linear, τ_0, h_0, and power law hardening, eq. (19), with two parameters, γ_{ref}, m, for tensile twinning. This adds up to $2 + 2{\times}3 + 4 = 12$ parameters for direct hardening, see Table 3. Latent hardening is described by $4 \times 4 = 16$ interaction parameters, $q_{\alpha\beta}$, see Table 4.

Table 3: Direct hardening parameters, calibrated using experimental data of Kelley and Hosford (1968a, b)

	basal $\langle \mathbf{a} \rangle$	prismatic $\langle \mathbf{a} \rangle$	pyramidal $\langle \mathbf{a} + \mathbf{c} \rangle$	tensile twinning
hardening law	Linear eq. (17)	Voce eq. (18)	Voce eq. (18)	linear + power law eqs. (17), (19)
τ_0 [MPA]	1	20	40	5
τ_∞ [MPA]	-	150	260	-
h_0 [MPA]	10	7500	7500	200
γ_{ref} [-]	-	-	-	0.11
m [-]	-	-	-	10

Table 4: Interaction (latent hardening) parameters, $q_{\alpha\beta}$, calibrated using experimental data of Kelley and Hosford (1968a, b)

α \ β	basal $\langle \mathbf{a} \rangle$	prismatic $\langle \mathbf{a} \rangle$	pyramidal $\langle \mathbf{a} + \mathbf{c} \rangle$	tensile twinning
basal $\langle \mathbf{a} \rangle$	0.2	0.5	0.5	0.5
prismatic $\langle \mathbf{a} \rangle$	0.2	0.2	0.2	0.5
pyramidal $\langle \mathbf{a} + \mathbf{c} \rangle$	1.0	1.0	0.2	0.25
Tensile twinning	1.0	1.0	0.2	0.25

The parameters have been determined by fitting simulation results to the test data of Kelley and Hosford (1968a, b), namely plane-strain compression tests on single crystals of orientations **A** to **G**, see Table 2, and on specimens of orientations **LT**, **LS**, **TL**, **TS**, **SL**, **ST**, cut from a textured plate. Parameter identification has actually been a systematic

procedure of trial and error, benefiting from a deeper insight into deformation mechanisms being active in the respective orientations of the single crystals. Different deformation modes are activated in the single crystal tests depending on the respective orientations of specimens. This allows for selectively identifying the hardening parameters for a particular slip mechanism, provided that the respective mechanism is exclusively activated in the model. This requires that the latent hardening parameters have values different from zero. The discussion of the simulation results below will elucidate this more clearly. The actual values of the latent hardening parameters cannot be concluded from the single crystal tests, however, but calls for the polycrystal test results. Due to the small number of grains used in the respective simulations and the merely qualitative mapping of the texture, only approximate predictions of the specimens' deformation behavior can be expected.

A comparison of simulation and test results for single crystals of orientations **A** to **G**, see Table 2, is shown in Fig. 5. Beside a general qualitative agreement between experimental and simulated results, the simulations capture the following specific features:

- Nearly identical stress-strain curves with high yield stress and strong hardening for orientations **A** and **B**, where the loading direction is $\langle 0\,0\,0\,1 \rangle$;

- Nearly identical stress-strain curves with - compared to **A** and **B** - lower yield stress for orientations **C** and **D**, where the constraint direction is $\langle 0\,0\,0\,1 \rangle$;

- Anomalous hardening behavior of orientations **E** and **F** with relatively low yield stress and almost no hardening at strains smaller than 6%, followed by a sudden increase in stress,

- Saturation stress of orientation **E** exceeding that of **A** and **B**.

- Saturation stress of orientation **F** about that of **C** and **D**.

- Very low stress level for orientation **G**.

The simulated stress increase in orientation **F** is delayed compared to that obtained in the tests. As the simulations aimed at a unique set of model parameters, this deviation between test results and model predictions has been accepted. Note also, that the

occurrence of stress rising for orientation **E** is not unambiguous in the tests, either. Considering the general assumptions made with respect to the hardening laws and the considerably large number of hardening parameters summarized in Table 3, the accordance between test and simulation results is considered as quite good.

The numerical simulations allow also for an analysis of the slip mechanisms causing the deformation of the single crystal samples. Fig. 6 shows the evolution of the relative activities of the various slip systems with increasing strain for each test. Relative activity indicates the contribution of a specific deformation mode to the plastic strain increment, as the latter is set to 1. Assuming non-zero values for the latent hardening parameters, the activation of the deformation modes for the different orientations occurs selectively. Only the curves **A** and **B** show more than one family of slip mechanisms acting at the same time, namely prismatic and pyramidal slip. Curves **C** and **D** are dominated by prismatic slip and curve **G** by basal slip over the whole range of strain. For orientations **E** and **F** the transition from twinning to pyramidal slip occurs within a very small range of strains. Orientations **E** and **F** favor plastic deformation resulting in an elongation of the c-axis. Because of its low critical resolved shear stress (CRSS), τ_0, tensile twinning is easily activated, and as saturation according to the power law eq. (19) occurs, elastic deformation increases the stresses until they reach the CRSS of pyramidal glide, which explains the sudden increase of stresses at about 0.06 strain in Fig. 5. This selectivity in the activation of slip mechanisms facilitates an efficient determination of the CRSS and the hardening parameter values of the different slip systems.

The comparison of Kelley and Hosford's (1968b) plane-strain compression tests on polycrystalline samples with orientations **LT, LS, TL, TS, SL, ST**, cut out of Mg rolled plates with the simulation results is depicted in Fig. 7. The two letters denote the orientation with respect to the loading and the constraint direction, respectively; L is the longitudinal or rolling direction, T the transverse and S the short transverse or thickness direction. The general trend is well reproduced for all curves except for curve **LT** where hardening is too small compared to the experimental data. Due to the rolling process, the c-axes of the grains are orientated approximately parallel to the thickness direction of the plate with a slightly higher deviation in rolling than in transverse direction. This pronounced texture results in some qualitative similarities, of the flow curves between

single crystals, Fig. 5, and polycrystals, Fig. 7. Polycrystals of orientations **LT**, **TL**, **ST**, **SL** show a monotonous hardening as the single crystals of orientations **A**, **B**, **C**, **D**. Those of orientations **TS** and **LS** exhibit the same striking hardening behavior as the single crystals of orientations **E** and **F**, namely relatively low yield stresses and little hardening at strains smaller than 4%, followed by a sudden increase in stress. Some differences of the hardening behavior of the polycrystals to that of single crystals are worth mentioning, however. The texture difference between the L and T orientation of the polycrystals is minor, see Fig. 4, which levels the differences between the respective curves in Fig. 7. The saturation stresses reached in the polycrystal specimens of orientations **ST** and **SL** are lower than those of the single crystals of orientations **A**, **B** , **C** and **D**, respectively, and the differences in the stresses of **LS** and **TS** are smaller than those between **E** and **F**. The curves **A**, **B**, **C**, **D** in Fig. 5 saturate, whereas the curves **LT** and **TL** in Fig. 7 do not. The specific shapes of the flow curves can be understood by the analysis of activated slip systems discussed below.

Despite the qualitative similarities in the hardening behavior between single crystals and textured polycrystals, the test data from polycrystals have great importance for the calibration of the material parameters, particularly the latent hardening parameters, $q_{\alpha\beta}$. Due to the varying orientations of grains in the RVE, more than one deformation mode has to be activated at the same time. This is manifested by Fig. 7, which shows the "integral" activity of the respective slip systems in the RVE. The above statement even holds on the level of a material point, where (different from the single crystal case) several slip mechanism are active. Hence, the latent hardening parameters affect the macroscopic response of the sample significantly and have to be identified from the tests on polycrystals rather than on single crystals.

The relative activation of slip systems shown in Fig. 8 helps in understanding the flow curves of Fig. 7. In the specimens of orientations **LT** and **TL**, about 60% of the plastic deformation results from prismatic slip with Voce hardening ($\tau_0 = 20$ MPa, $\tau_\infty = 150$ MPa), nearly 30% from basal slip with linear hardening ($\tau_0 = 1$ MPa). For the specimens of orientations **SL** and **ST**, pyramidal (Voce hardening, $\tau_0 = 40$ MPa, $\tau_\infty = 260$ MPa) and basal slip (linear hardening) contribute nearly equally by about 40% and prismatic slip (Voce hardening, $\tau_0 = 20$ MPa , $\tau_\infty = 150$ MPa) by about 20%. The low

yield strength and hardening for the orientations LS and TS is due to the activation of tensile twinning ($\tau_0 = 5$ MPa), which contributes to the plastic deformation by about 40%, and the sudden increase of stresses beyond 5% strain results from the saturation of twinning going along with the activation of pyramidal slip.

Yield Surfaces of Polycrystals

Simulations of the structural behavior of polycrystals cannot be performed effectively with crystal plasticity models on the microscale but require phenomenological constitutive equations for yielding and hardening under multiaxial stress states. These equations are established on a meso level. In micromechanical modeling, the transfer from the micro to the mesoscale is performed by representative volume elements (RVEs), which are designed to represent typical periodic microstructures of polycrystalline materials.

Kelley and Hosford (1968b) have determined yield loci in the (L,T)-plane of rolled plates experimentally for varying levels of the largest principal strain, ε_I, as 1, 5, 10%, using the experimental results presented in Fig. 7 as well as uniaxial tension and compression tests in L-,T- and S-direction. A comparison of test and simulation results is presented in Table 5.

Table 5: Yield stresses of textured polycrystalline specimens in L-, T-, and S-orientation at three strain levels under uniaxial tension and compression; comparison of test results (Kelly and Hosford, 1968b) with results of RVE simulations

	1% principal strain		5% principal strain		10% principal strain	
	test	sim.	test	sim.	test	sim.
L-tens. [MPa]	68.3	94.2	100.0	162.0	-	190.8
S-comp. [MPa]	66.2	91.7	127.6	166.1	147.5	181.0
T-tens. [MPa]	129.6	123.4	173.7	198.9	194.4	214.4
L-comp. [MPa]	26.9	27.1	54.5	81.2	146.2	159.4
T-comp. [MPa]	28.3	52.8	71.7	102.7	172.4	203.5

The simulated stresses in Table 5 overestimate the experimental ones considerably in

almost all loading configurations and at all strain levels. This appears very much like a systematic error, too pronounced for being wiped off. The effect of boundary conditions and friction has been investigated by the authors and found to be of less significance. Any other explanation for the observed misfit is still missing. Nevertheless, the two most notable aspects of the yield behavior for magnesium plates are reproduced by the simulations, namely anisotropy and tension/compression asymmetry. In view of a number of approximations and imponderabilities in the simulations, particularly with respect to the parameter identification and the mapping of the texture, as well as possible uncertainties in the evaluation of the test data, the coincidence of experimental and numerically simulated tests is satisfying and encouraging for the generation of qualitatively realistic yield surfaces of the plate material.

Fig. 9 shows subsequent yield surfaces for mesoscopic stresses under increasing equivalent plastic strain from $\varepsilon^p = 0.01$ to 0.10 with an increment of 0.01. Though the authors are aware that von Mises equivalent strain is obviously not an appropriate measure for characterizing the mesoscopic hardening, they chose it nevertheless lacking a more adequate one. At low values of plastic strain the RVE exhibits a strong anisotropy and a high asymmetry of yielding between tension and compression while, with increasing plastic strain the anisotropy and yielding asymmetry reduce considerably.

The evolution of the accumulated shear strain of the four slip systems in the RVE is presented in Fig.10 in dependence on the angle, ρ, of the loading path. The contributions of basal and prismatic slip oscillate with a period of approximately 180° and a phase shift of about 90° to each other. Both deformation modes act equally in tension and compression. The phase shift of 90° points out that both, basal and prismatic slip act in $\langle \mathbf{a} \rangle$ direction and compete with each other. Even though the texture of a rolled plate is not actually favorable for basal slip, it is, in average over the whole range $\rho \in \left[0°, 360° \right]$, the most active deformation mode due to its extremely low CRSS. Interestingly, the relative contribution of basal slip to the accumulated shear strain tends to decrease with increasing strain while that of the prismatic slip tends to increase. This is probably also related to difference in CRSS for both deformation mechanisms implying that basal slip is more active at the beginning of the deformation, where stresses are lower, than at the end, and prismatic slip becomes more active at higher strains. As expected, tensile twin is

activated between $120° < \rho < 330°$, only, where compression is present and, due to the texture, elongation in c-direction is favored. The highest twinning activity is concentrated in the range between $180° < \rho < 270°$, where compression states exist in both longitudinal and tangential direction of the plate. Pyramidal slip is significantly active in the range between $0° < \rho < 90°$, where shortening along the c-axis is favored. Following the same principle as in orientations **E** and **F** in Fig. 5, as well as **LS** and **TS** in Fig. 7, pyramidal slip $\langle \mathbf{a} + \mathbf{c} \rangle$ between $120° < \rho < 330°$, is absent at low strains and activated at higher strains once twinning saturates.

Phenomenological Yield Potential

As stated above, phenomenological constitutive equations for yielding and hardening are required for simulations of the macroscopic structural behavior. The numerially generated isocontours shown in Fig. 9, have hence to be fitted by an analytical expression of the yield potential and an evolution equation for this yield potential has to be established. A phenomenological yield potential for textured magnesium has to account for both anisotropy and tension/compression asymmetry. Hill (1948, 1950) has generalized the von Mises (1913) criterion for anisotropic materials. It predicts yield loci, however, which are centered about the origin, and is hence not suited for hcp metals deforming primarily by twinning. Accounting for the asymmetry of yielding in tension and compression, that is shifting the center of the yield surface out of the origin of the deviatoric plane, requires including the third invariant of the stress tensor (Drucker, 1949),

$$f^0 \equiv \left(J_2^0 \right)^{\frac{3}{2}} - c J_3^0 = \tau_Y^3 . \tag{23}$$

Cazacu and Barlat (2004) have shown, that this yield criterion describes well the asymmetry of yielding due to activation of twinning. J_2^0 and J_3^0 are generalizations of the second and third invariant of the stress tensor for orthotropic materials, containing 6 and 11 model parameters, respectively, in the general three-dimensional case. The total number of model parameters reduces to 7 in the plane stress case. Different from the yield criteria of von Mises and Hill, convexity of the yield surface is not a priori ensured and has therefore to be introduced as an additional side condition, while identifying the

respective parameters, in order to fulfill Drucker's postulate of material stability (Drucker, 1964). The respective investigations based on the micromechanically yield surfaces of Fig. 9 are in progress.

CONCLUSIONS

A crystal plasticity model has been used to study the deformation mechanisms of an hcp metal. Simulations of plane-strain compression tests and uniaxial tension and compression tests revealed that the experimentally observed phenomena of magnesium and its alloys, namely a strong anisotropy and a significant tension/compression asymmetry, can be understood considering four deformation mechanisms and their activation: three basal slip systems, three prismatic slip systems, six pyramidal slip systems and six tensile twinning systems. Twinning has clearly been identified for being responsible for the tension-compression asymmetry which is observed in textured rolled plates. Material parameters have been calibrated based on single crystal and polycrystal experiments.

Once the material parameters of crystal plasticity have been identified, they can be used for predicting the mechanical response of arbitrarily textured polycrystalline materials by building aggregates of single crystals. The respective transfer from the microstructure to a phenomenological representation of yielding of polycrystalline samples has been successfully verified. Establishing a phenomenological yield potential and a respective hardening rule for hcp materials is the future step in the modeling chain. The presented methodology links investigations on the micro-level with simulation techniques used on the lengthscale of engineering structures. Hence it can be understood as a link between micro- and macromechanics.

REFERENCES:

Agnew, S. R., Duygulu, ö., 2005. Plastic anisotropy and the role of non-basal slip in magnesium alloy AZ31B 21. Int. J. Plasticity 21, 1161-1193.

Agnew, S. R., Tomé, C. N., Brown, D. W., Holden, T. M., Vogel, S. C., 2003. Study of slip mechanisms in a magnesium alloy by neutron diffraction and modeling. Scripta Materialia 48, 1003-1008

Agnew, S. R., Yoo, M. H., Tomé, C. N., 2001. Application of texture simulation to understanding mechanical behavior of Mg and solid solution alloys containing Li or Y. Acta Mater. 49, 4277-4289

Ando, S., Tonda, H., 2000. Non-basal slip in magnesium-lithium alloy single crystals, Mater. Trans. JIM 41, 1188-1191

Asaro, R.J., 1983, Crystal plasticity. J. Appl. Mech. 50, 921-934

Asaro, R. J., 1983. Micromechanics of crystals and polycrystals. Adv. Appl. Mech. 23, 1-115

Beck, A., 1939. Magnesium und seine Legierungen, Springer, Berlin

Brocks, W. , Steglich, D. (2006). Hybrid methods. In: Comprehensive Structural Integrity - Fracture of Materials from Nano to Macro, Volume 11: Mechanical Characterization of Structural Materials, Elsevier, to be published

Cazacu, O., Barlat, F., 2004. A criterion for description of anisotropy and yield differential effects in pressure insensitive materials. Int. J. Plasticity 20, 2027-2045

Drucker, D. C., 1949. Relation of experiments to mathematical theories of plasticity. J. Appl. Mech. 16, 349-357

Drucker, D. C., 1964. On the postulate of stability of material in the mechanics of continua. Journal de Mécanique 3, 235-249

Göken, J., Bohlen, J., Letzig, D., Brokmeier, H.-G., Kainer, K.-U., 2002. Mg-Feinbleche für den Ultraleichtbau in der Verkehrstechnik. In: Kaufmann H., Uggowitzer, J. P., Wahlen, A., (Eds.), 2 Ranshofener Leichtmetalltage 2002 - Vom Werkstoff zum Bauteilsystem, LKR-Verlag, 229-240

Hauser, F. E., Landon, P. R., Dorn, J. E., 1956. Deformation and fracture mechanisms of polycrystalline magnesium at low temperatures. Transactions of the ASM 48, 986-1002

Hill, R., 1966. Generalized constitutive relations for incremental deformation of metal

crystals by multislip. J. Mech. Phys. Solids 15, 95-102

Hill, R., 1948. A theory of the yielding and plastic flow of anisotropic metals, Proc. R. Soc. Lond. A 193, p. 281-297

Hill, R., 1950. The Mathematical Theory of Plasticity, Oxford University Press (Chapter XII), 317-340

Hill, R., Rice, J. R., 1972. Constitutive analysis of elastic-plastic crystals at arbitrary strain. J. Mech. Phys. Solids 20, 401-413

Huang, Y., 1991. A user-material subroutine incorporating single crystal plasticity in the ABAQUS finite element program, Report MECH-178. Div. Applied Science, Harvard University, Cambridge (MA)

Kainer, K.-U., (Ed.), 2003. Magnesium Alloys and Their Applications, Wiley-VCH, Weinheim

Kelley, E. W., Hosford, W. F., 1968a. Plane-strain compression of magnesium and magnesium alloy crystals. Transactions of the metallurgical society of AIME 242, 5-13

Kelley, E.W., Hosford, W.F., 1968b. The deformation characteristics of textured magnesium. Transactions of the metallurgical society of AIME 242, 654-661

Mahnken, R. (2004). Identification of material parameters for constitutive equations. In: Encyclopedia of Computational Mechanics (ed. E. Stein, R. de Borst and Th.J.R. Hughes) John Wiley & Sons, Chichester , 637-655

Neelameggham, N. R., Kaplan, H. I., Powell, B. R., (Eds.), 2005. Magnesium Technology 2005, Publication of TMS

Obara, T., Yoshinga, H., Morozumi, S., 1973. $\{11\bar{2}2\}\langle\bar{1}\,\bar{1}23\rangle$ slip system in magnesium. Acta Metall. 21, 845-853

Peirce, D., Asaro, R. J., and Needleman, A., 1982. An analysis of nonuniform and localized deformation in ductile single crystals. Acta Met. 30, 1082-1119

Reed-Hill, R. E., Robertson, W. D., 1957. Deformation of magnesium single crystals by non basal slip. Journal of metals. Transactions AIME, 496-502

Rice, J. R., 1971. Inelastic constitutive relations for solids: an internal variable theory and its application to metal plasticity. J. Mech. Phys. Solids 19, 433-455

Staroselsky, A., Anand, L., 2003. A constitutive model for hcp materials deforming by

slip and twinning: application to magnesium alloy AZ31B. Internationnal Journal of Plasticity 19, 1843-1864

Styczynski, A., Hartig, Ch., Bohlen, J., Letzig, D., 2004. Cold rolling textures in AZ31 wrought magnesium alloy. Scripta Materialia 50, 943-947

Stohr, J. F., Poirier, J. P., 1972. Etude en microscopie electronique du glissement pyramidal (11-22) (11-23) dans le magnesium, Phil. Mag. 25, 1313-1329

Taylor, G. I., 1938. Plastic strain in metals. J. Inst. Metals 62, 307-324

Tegart, W. J. McG., 1964. Independent Slip Systems and Ductility of Hexagonal Polycrystals. Phil. Mag. 9, 339-341

von Mises, R., 1913. Die Mechanik der festen Körper im plastischen deformablen Zustand. Nachr. Ges. Wiss., Göttingen, 582-592

von Mises, R., 1928. Mechanik der plastischen Formänderung von Kristallen. Z. angew. Math. u. Mech. 8, 161-185

Wonsiewicz, B. C., Backofen, W. A., 1967. Plasticity of magnesium crystals. Transactions of the metallurgical society of AIME 239, 1422-1431

Yi, S. B., Davies, C. H. J., Brokmeier, H.-G., Bolmaro, R. E., Kainer, K.-U., Homeyer, J., 2006. Deformation and texture evolution in AZ31 magnesium alloy during uniaxial loading. Acta Materialia 54, 549-562

Yoshinaga, H., Horiuchi, R., 1963. On the nonbasal slip in magnesium crystals. Trans. JIM 5, 14-21

FIGURES
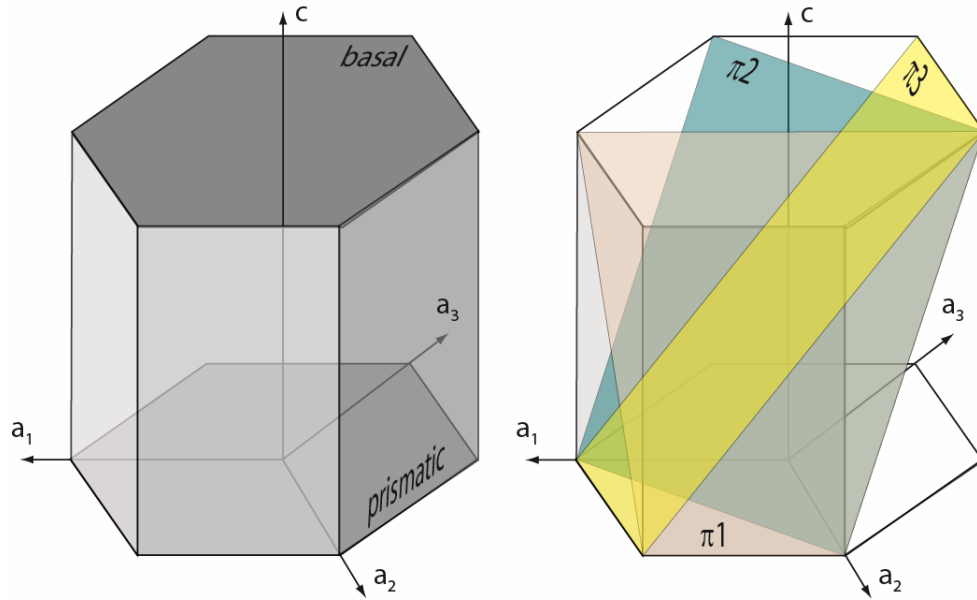
Figure 1: Slip planes in hcp material: basal and prismatic planes (left), pyramidal (π1: $\{01\bar{1}1\}$, π2: $\{11\bar{2}2\}$, π3: $\{10\bar{1}2\}$) planes (right)
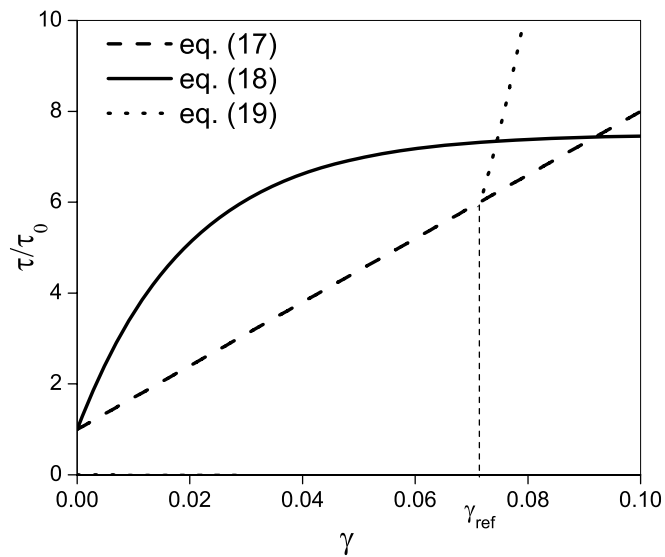

Figure 2: Hardening laws used in the present investigations
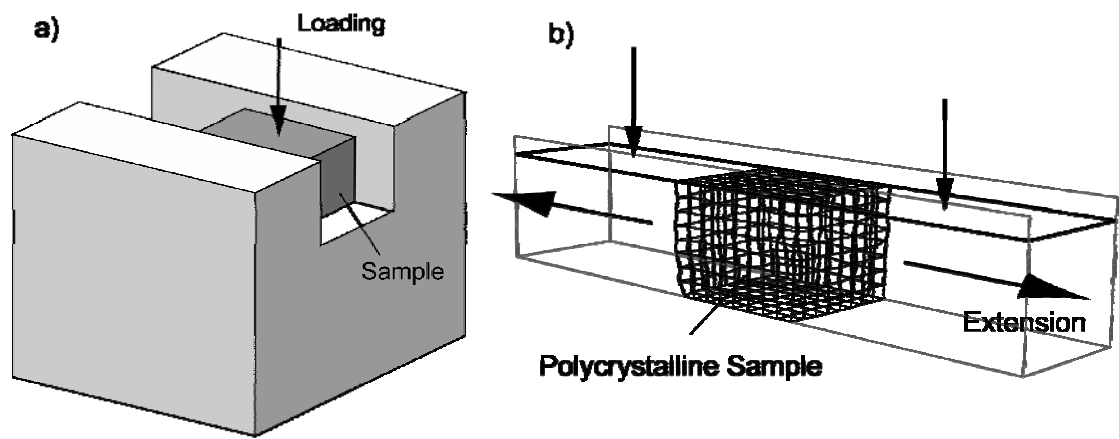
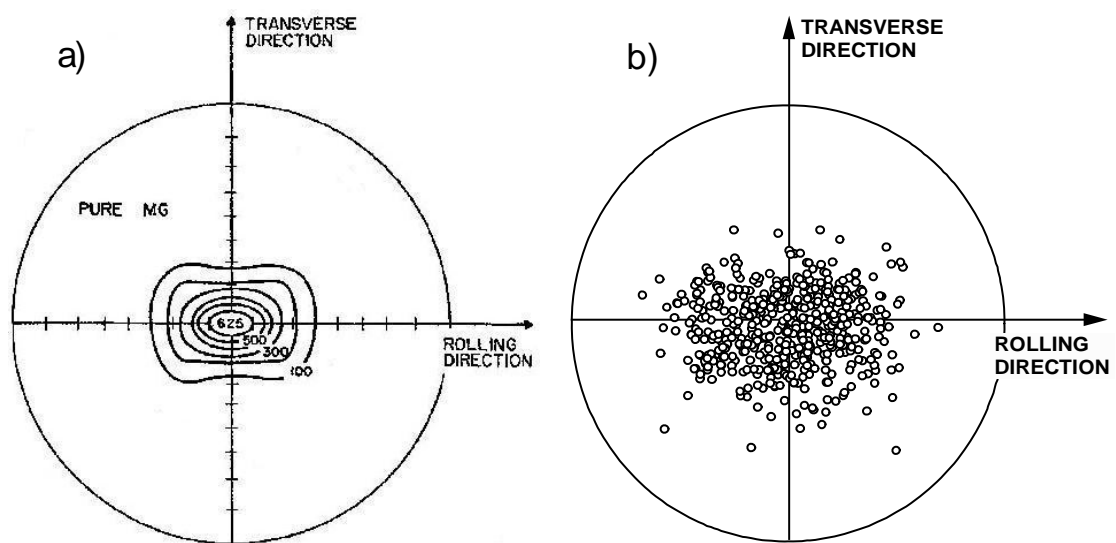Figure 3: Plane-strain compression test: principle (a) and FE model of a polycrystal (b)

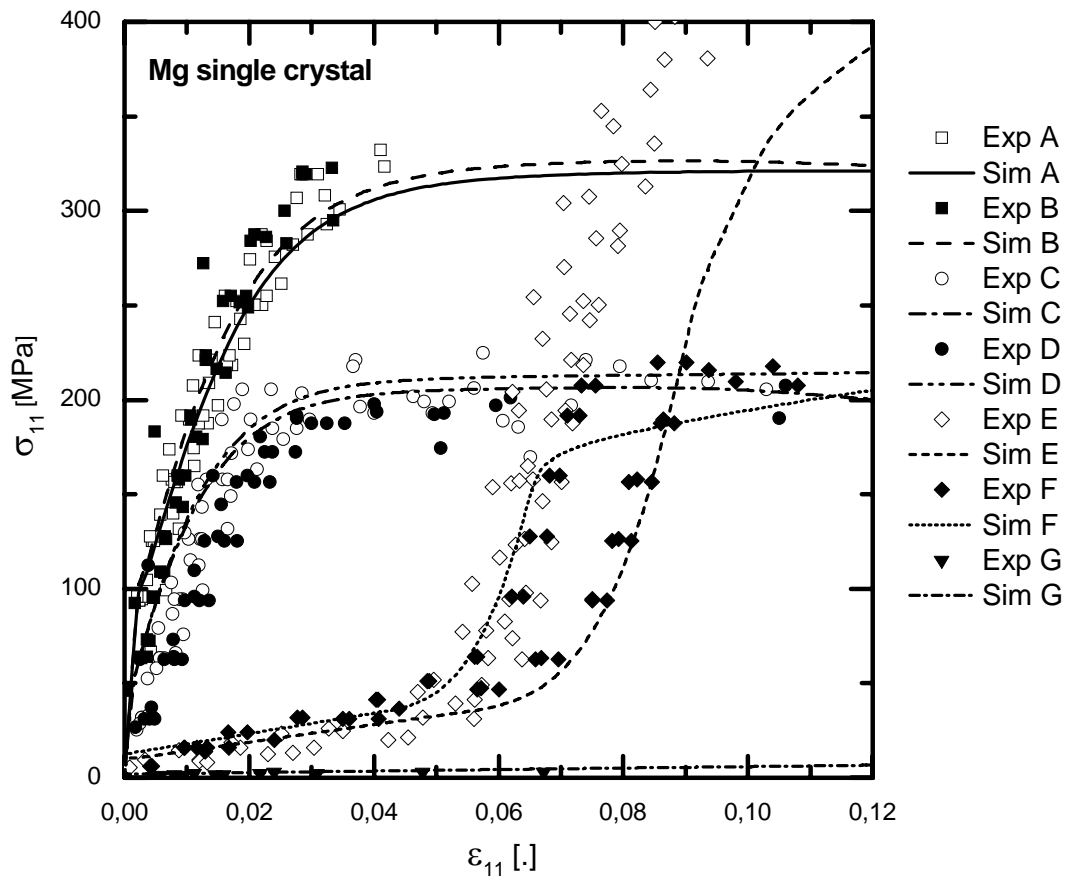Figure 4: Experimental (Kelly and Hosford, 1968b) (a) and simulated (0001) pole figures (b) of pure magnesium rolled plate material
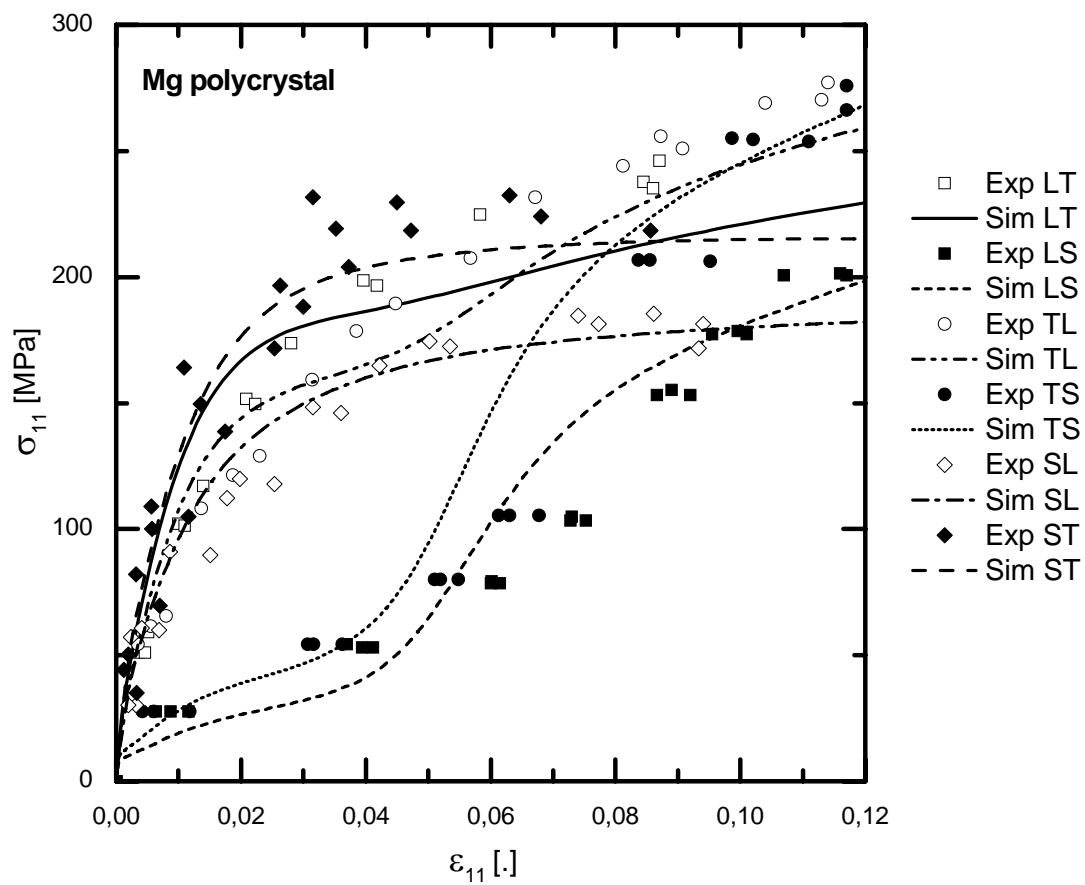
<u>Figure 5</u>: Plane-strain compression tests of pure Mg single crystal: simulation results and tests (Kelly and Hosford, 1968a).
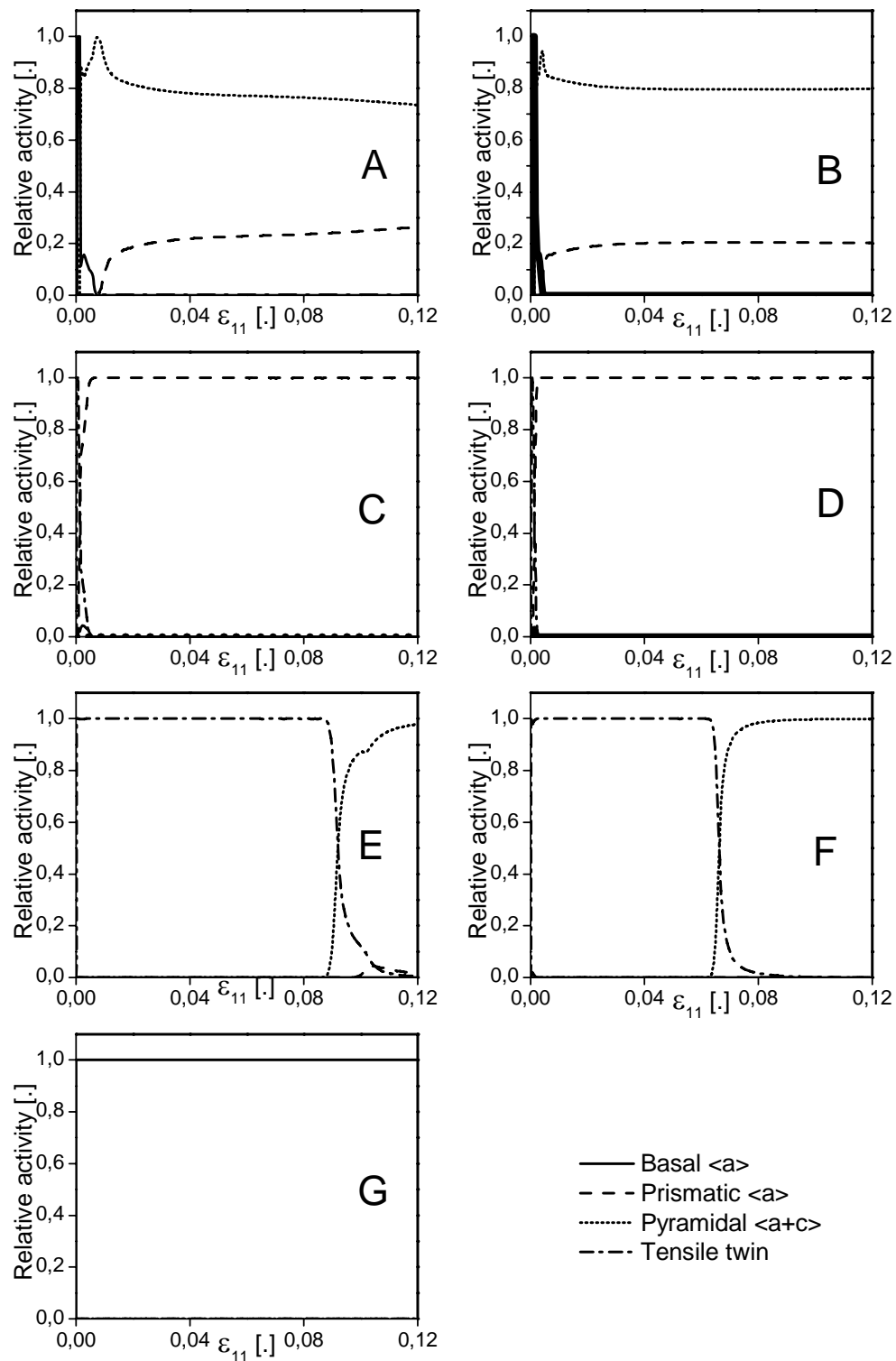
Figure 6: Relative activity of slip mechanisms in dependence of the initial crystallographic orientation of the specimens in simulated channel die tests of Mg single crystals

Figure 7: Plane-strain compression tests of textured Mg rolled plate material, simulation results and tests (Kelly and Hosford, 1968b).
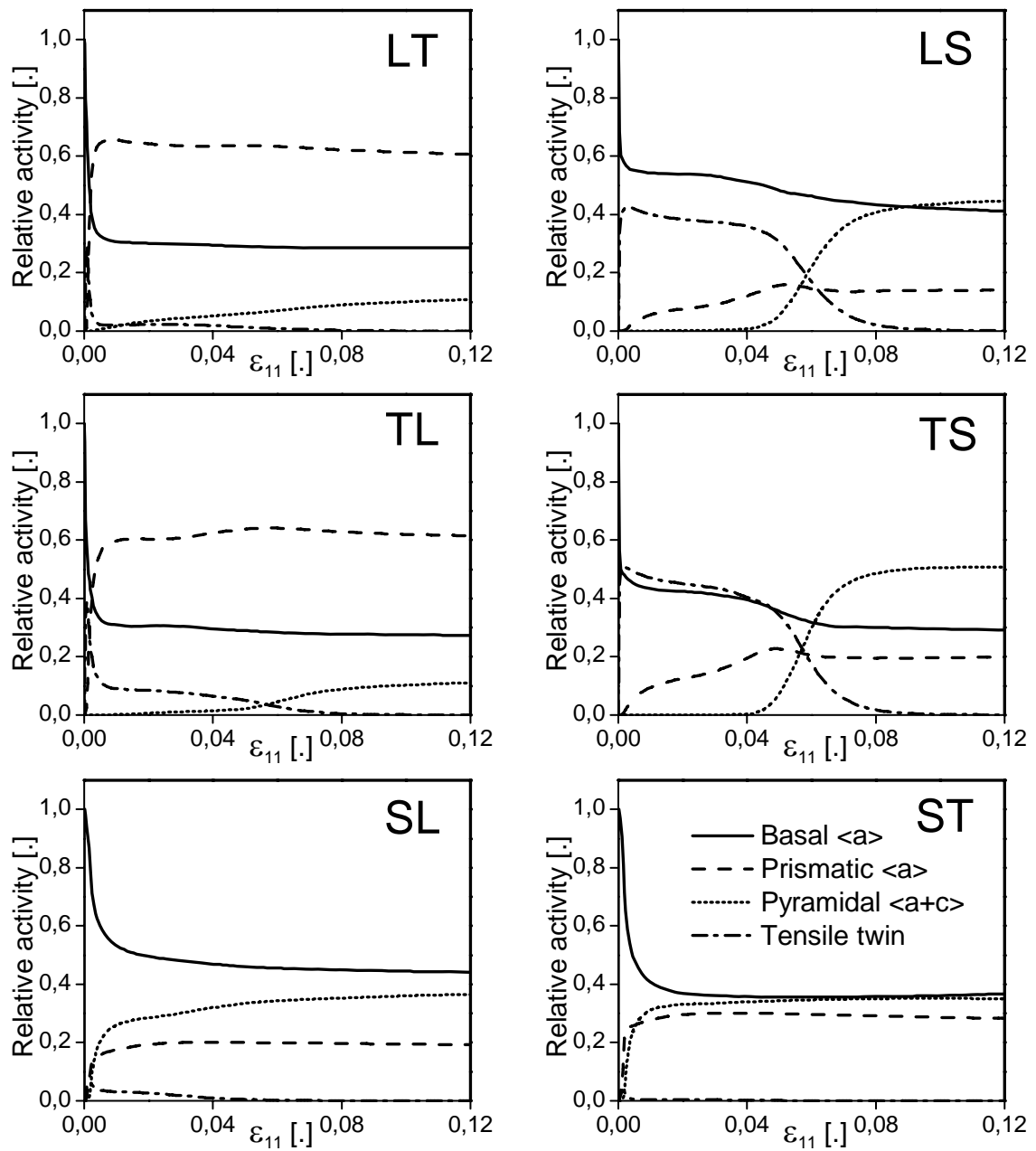
<u>Figure 8</u>: Relative activity of slip mechanisms in dependence on the initial orientation of the specimens in simulated channel die tests of textured Mg rolled plate samples
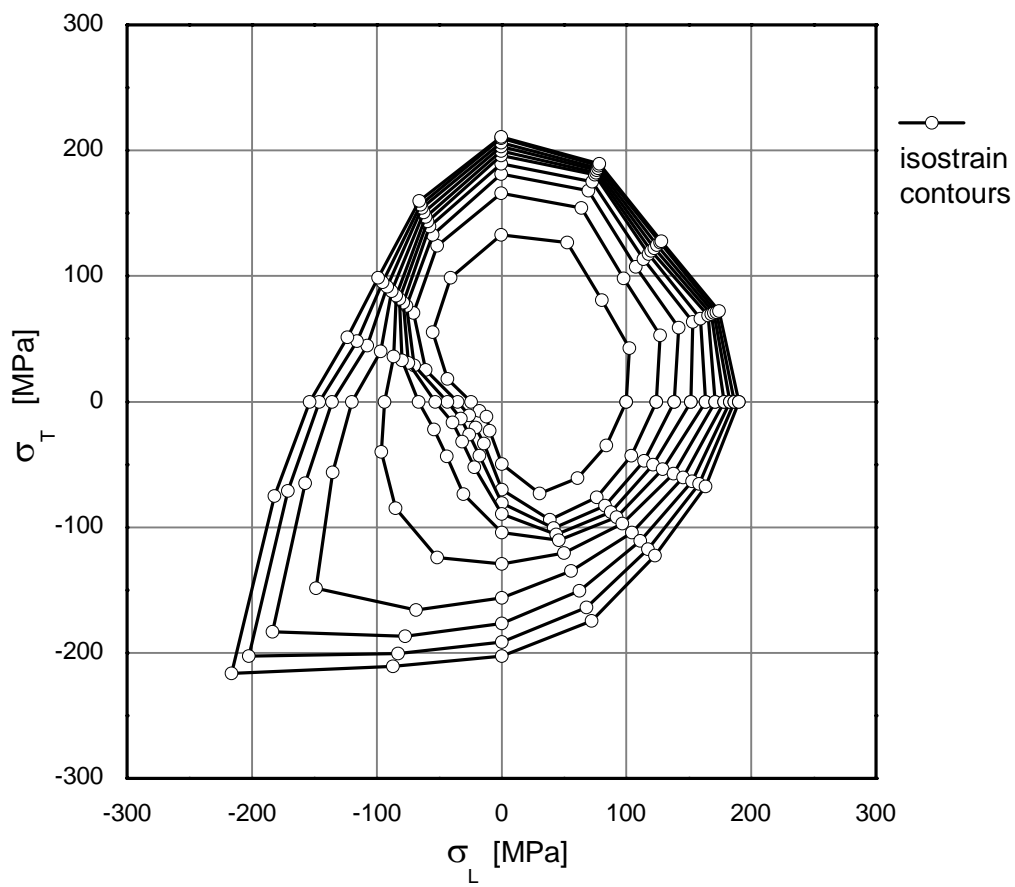
Figure 9: Iso-contours of current mesoscopic yield stress of a textured polycrystalline RVE under plane-stress biaxial loading (ε^p =0.01, …, 0.1)
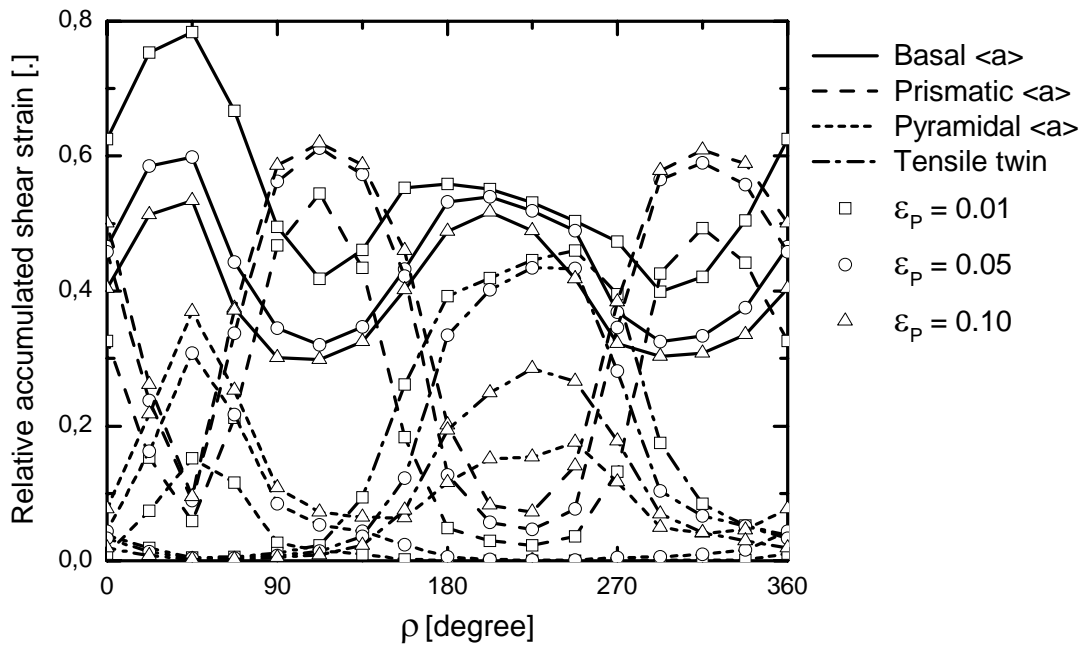
Figure 10: Contributions of crystallographic deformation modes at 0.01, 0.05, and 0.1 equivalent plastic strain for plane-stress biaxial loading of a textured polycrystalline RVE